

Unravelling the Excitation Spectrum of the Nucleon

A.M. Sandorfi

Physics Division, Thomas Jefferson National Accelerator Facility, Newport News, VA 23606, USA

Email: sandorfi@JLab.org

Abstract. The low-energy structure of QCD lies encoded in the excited states of the nucleon, a complicated overlap of many resonances. Recent Lattice calculations have confirmed the long-standing quark model predictions of many more excited states than have been identified. Reactions that probe the spectrum are clouded by effects that *dress* the interactions and complicate the identification of excited levels and the interpretation of their structure. Recent theoretical work has exposed dramatic effects from such *dressings*. On the experimental side, new *complete* measurements of pseudoscalar meson photo-production are being pursued at several laboratories, where here the designation of *complete* refers to measurements of most if not all of the 16 possible reaction observables. This has been the focus of a series of experiments at Jefferson Lab culminating in the recently completed g9/FROST and g14/HDice runs which are now under analysis. With realistic errors, the number of observables needed to constrain the production amplitude is many more than required of a *mathematical* solution.

1. Quark Models and Lattice Calculations

A successful description of the excited levels of a composite system is a basic test of how well the underlying forces are understood. While Quantum-Chromodynamics (QCD) is generally regarded as a relatively mature theory describing the interactions of quarks within hadrons, the excited states of the nucleon pose many challenges. This partly arises because of the ways in which the spectrum, as well as the decay widths of excited levels, are influenced by the underlying nature of quark confinement and Chiral Symmetry breaking, and partly because of multiple effects that *dress* the interactions and alter their manifestation. This paper discusses some of the features and puzzles associated with excited nucleons and describes a new experimental initiative aimed at unfolding the nucleon spectrum through measurements of *everything*.

Quark models have been very successful at capturing the symmetries of QCD without solving its Lagrangian. In such models, a nucleon has 3 *constituent* quarks with masses of about 0.3 GeV. At the same time the *current* quarks of deep-inelastic scattering have energies of at most a few MeV. Recent theoretical calculations comparing QCD on a Lattice with solutions of the Dyson-Schwinger equations (DSE) have provided the connection between these two successful but very different pictures [1]. Figure 1 shows the running quark mass, dressed by gluons, as a function of momentum. The descending sets of points are Lattice-QCD (LQCD) calculations that start with different current quark masses in the perturbative regime, as indicated in the legend to the right of the plot, the lowest being a linear extrapolation to the Chiral limit of zero. The curves are the corresponding DSE results. The accumulation of effective mass below about 1 GeV/c arises from a cloud of gluons that are dragged along with the quark as it propagates. The IR inflection that is evident in the DSE curves below about $\frac{1}{4}$ GeV/c results from Dynamical Chiral symmetry breaking and is the signature of quark confinement.

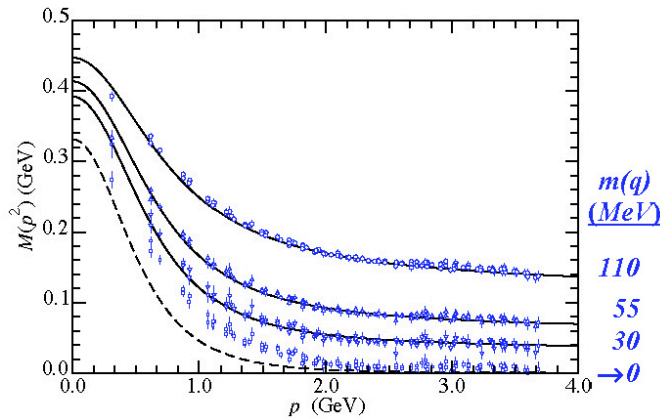


Figure 1. Effective quark mass as a function of momentum, from [1]. Descending sets of Lattice QCD points correspond to calculations with different assumptions for the current quark mass, as indicated to the right. The solid curves are the corresponding Dyson-Schwinger calculations. The *constituent* mass appears at low momentum from the gluon cloud.

The results of figure 1 have provided the anticipated connection between the constituent mass of *QCD-inspired* models, which on the whole are quite successful, and the current quarks of QCD. Specifically, it is the gluon cloud, emerging from the dynamical breaking of Chiral symmetry, that generates *constituent* quarks with effective masses and the essential features captured in quark models.

A long-standing prediction of constituent quark models (CQM) is the expectation of many more N^* levels than have been observed. The predicted spectrum from Capstick and Roberts [2] is reproduced in the left panel of figure 2. Candidate πN resonances assigned a 3 or 4-star status by the Particle Data Group are circled. Only the lowest few states in each oscillator band correspond to observed resonances.

A traditional model approach to the apparent paucity of identified N^* resonances has been to invoke mechanisms that effectively reduce the number of degrees of freedom. Diquark correlations, in which two quarks are coupled to a *point-like*, spin 0 and isospin 0 object, have been employed for some decades. By freezing out internal diquark excitations the number of predicted levels are reduced significantly [3]. However, more recent calculations with the Dyson-Schwinger equations have shown that diquark correlations, which are indeed energetically favored and hence very likely, have about the radius of a pion [4]. Thus internal diquark excitations are not expected to be frozen out.

Recent LQCD predictions from the *Hadron Spectrum Collaboration* [5] are shown for comparison in the right panel of figure 2. These LQCD calculations include all possible $q-q$ correlations and still yield a large number of as yet to be discovered N^* states. In short, *diquarks can no longer be regarded as a solution to missing N^* states*. With this LQCD validation of predictions for a plethora of higher

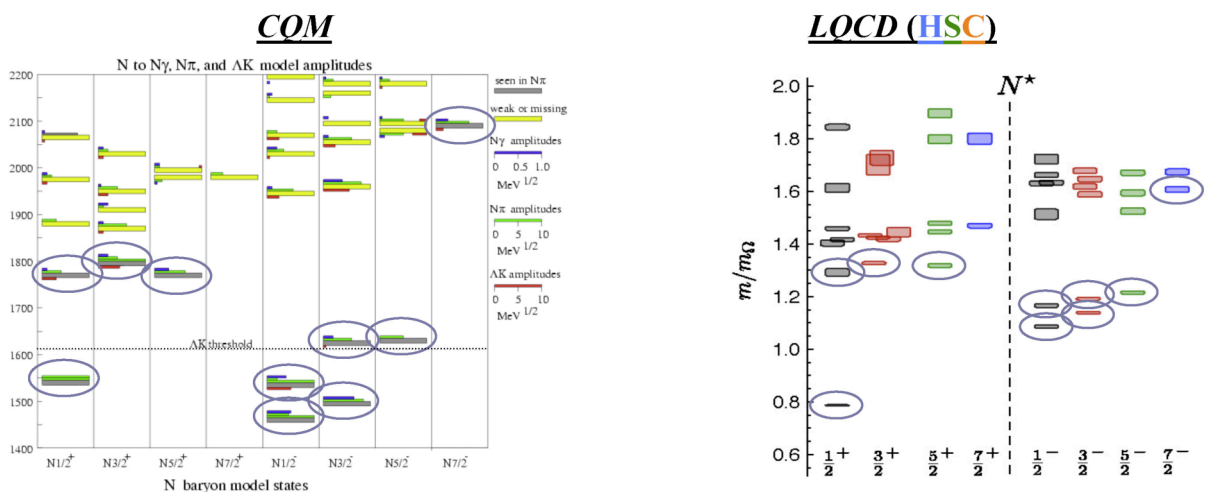


Figure 2. The N^* spectrum as predicted by the CQM (left panel), adapted from [2], compared with LQCD predictions (right panel) from [5]. Candidate πN resonances with 3 or 4-star status are circled.

lying levels, uncovering new resonances has become a high priority. Indeed, their absence at this point would pose serious problems.

2. Nature's Dressings

There are a number of factors that can complicate the search for new N^* levels. First of all, the CQM predicts (and by inference, the symmetry of the QCD Lagrangian expects) πN partial widths that diminish with energy. This may account for the difficulty in isolating signatures of higher lying N^* states in πN scattering data. Fortunately, these same higher lying states are expected to have larger branches to KY and $\pi\pi N$ final states. Such final states are excited in photo-production and the spin of the photon provides additional probes of the amplitude.

Further complications in comparing photo-production processes to a predicted spectrum enter through what are usually called *dressing* of the interaction vertices. We associate a *resonance* with a pole in an s -channel diagram, such as in figure 3. But a lot of detail is buried in the vertices. Models of



Figure 3. An s -channel pole excited through an electromagnetic vertex, with subsequent decay through the strong vertex.

the electromagnetic vertex must incorporate effects from the dynamical breaking of chiral symmetry which dresses the neutron and proton with a cloud of spin zero mesons (π , η , κ). For example, the photon of figure 3 can attach to a nucleon that is off-shell due to the presence of a virtual pion loop, or it can attach to the pion itself, etc. So the initial vertex is really an expansion. At the present level of sophistication, quark models do not include such pion clouds, so differences from measurement will be expected. In general, such mesonic *dressings* of the electromagnetic vertex affect the dynamical properties of a resonance and the Q^2 evolution of N^* production, but do not affect spectral properties.

The higher energies of the *missing* N^* levels are above thresholds for many decay channels. Hyperon channels, for example, can be either produced directly (eg. $\gamma p \rightarrow K\Lambda$) or reached through various two-step processes (eg. $\gamma p \rightarrow \pi N \rightarrow K\Lambda$). As a result, calculating the *strong* vertex of figure 3 becomes a multi-channel, multi-resonance problem, with Unitarity requirements connecting all possible channels. These *coupled-channel dressings* of the strong vertex essentially determine the spectral properties of N^* resonances – their mass/pole positions and widths.

We can illustrate the challenges and the fruits of detailed reaction analyses using the example of the $P_{11}(1440)$ Roper resonance, the nucleon's second excited level. This state has a complicated history and has long been shrouded in mystery. It was one of the first examples of a resonance that is not directly observable as a peak in a cross section, but rather required by detailed partial wave analyses (PWA) [6]. Recent PWA in fact suggest a doublet of closely spaced poles [7]. As a general rule, all calculations predict this state at too high an energy. It has been modeled mostly as either a 3-quark radial excitation (a nucleon *breathing mode*) or as a $qqq-g$ quark-gluon hybrid. These dynamical distinctions can be separated by studying the Q^2 evolution of the electro-production amplitude. The P_{11} decays into πN , $\pi\pi N$ and ΔN final states. The helicity amplitude for P_{11} electro-production is shown in figure 4 as a function of the square of the 4-momentum transfer (Q^2). Data from the CLAS detector at Jefferson Lab is plotted for both the πN (red circle) [8] and the $\pi\pi N$ (blue square) [9] final states. The green short-dashed curve gives the expected Q^2 dependence of a $qqq-g$ gluonic-hybrid excitation from [10]. This picture completely misses the cross-over in sign at around $\frac{1}{2} \text{ GeV}^2$ and can be ruled out. The shaded band shows the range of various quark-model calculations, adapted from [9]. These exhibit the change in sign at low Q^2 (a consequence of relativity) and the falling trend at high Q^2 , but appear shifted from the data. However, these quark models do not contain pion clouds. The expected contributions from the nucleon's virtual pion cloud are shown as the orange long-dashed curve [11] in figure 4 and are quite substantial. Combined with the appropriate phase, they can at least qualitatively

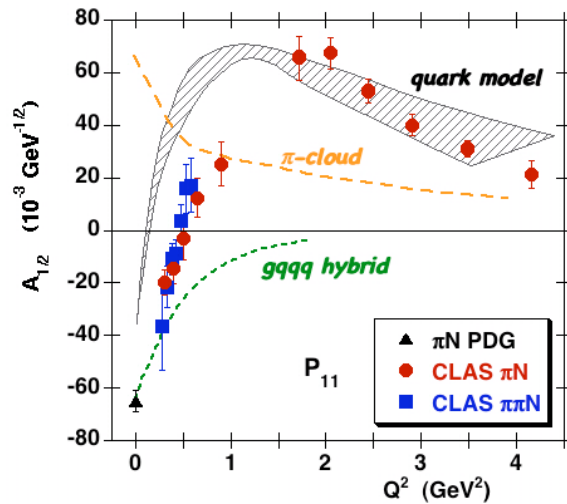


Figure 4. Helicity amplitudes for $P_{11}(1440)$ electro-production, deduced from πN (red circles) [8] and $\pi\pi N$ (blue squares) [9] final states. The short-dashed green curve gives the qqg quark-gluon hybrid expectation from [10]. The shaded band shows the range of various quark-model calculations, adapted from [9] and references therein. The expected contribution from the pion cloud is indicated as the orange long-dashed curve [11].

account for the shift in quark-model calculations that do not include meson clouds. In this way, Q^2 evolutions probe the photon vertex of figure 3 and provide valuable information on excitation mechanisms.

The meson-baryon dressings of the strong vertex of figure 3 can only be studied in combined simultaneous *coupled-channel* analyses that maintain Unitarity across many meson decay channels. Recent calculations from the group at the Excited Baryon Analysis Center (EBAC) at Jefferson Lab have used a dynamic coupled channel model to simultaneously describe γN and πN reactions leading to πN , $\pi\Delta$, ρN , σN , ηN , $K\Lambda$ and $K\Sigma$ final states. This calculation starts with a single *bare* N^* state (equivalent to a quark model level) in the P_{11} partial wave and analytically continues this into the complex plane. (Here, a grid search is carried out to find minima in the denominator of the T matrix as the strengths of the channel couplings are allowed to grow. In this way, trajectories in the complex plane are mapped out leading to poles on multiple Riemann sheets.) Their results for the poles in the final state P_{11} amplitude are shown in figure 5 [12]. As meson-baryon channel couplings are increased, what starts off as a bare quark excitation at 1763 MeV splits into a high-lying P_{11} state and a closely spaced doublet at the energy of the *Roper*, one dominated by the πN channel and the other by $\pi\pi N$. This doublet nature of the *Roper* resonance is in fact a common feature of all recent multipole analyses. In addition, it is now apparent why all previous N^* models had difficulty accounting for the low energy of the *Roper* resonance – the excitation of the quark core has to occur at a considerably higher energy in order to give the channel couplings the space to bring the apparent pole position(s) down to the energy of the experimentally observed resonance(s). In recent DSE calculations, this *bare* P_{11} is in fact generated by a radial excitation of a diquark, coupled to the third quark of the nucleon.

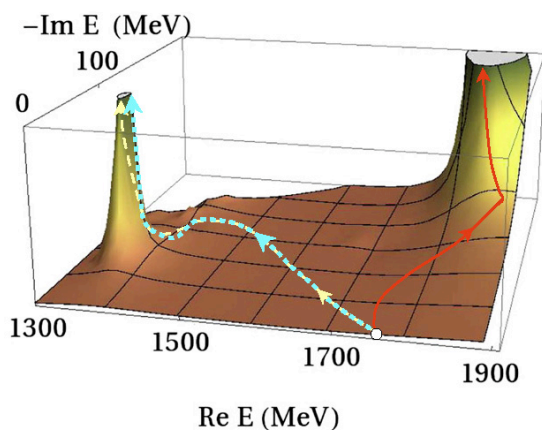


Figure 5. The trajectories and poles in the P_{11} amplitude, as calculated in the EBAC Dynamic Coupled-Channel model of meson production. (Adapted from [12].) Channel-couplings cause the *bare* N^* state at 1763 MeV to split into a high lying P_{11} and a doublet corresponding to the traditional *Roper* resonance.

3. Measurements of *Everything*

Single pseudo-scalar photoproduction is described by 4 complex amplitudes. A mathematical solution for the amplitude would require angular distribution measurements of at least 8 carefully chosen observables at each energy for both proton and neutron targets [13]. The lack of such experimental information, despite 50 years of photo-production measurements, has created ambiguities that could easily account for the difficulties in locating N^* resonances. To address this shortcoming, a sequence of *complete* experiments have been completed and are now under analysis at Jefferson Lab [14,15], as well as complementary experiments at Bonn and Mainz, with the goal of obtaining a direct determination of the amplitude to within a phase, for at least a few production channels.

In single-pseudoscalar meson photoproduction there are 16 possible observables, the cross section (σ), three asymmetries which to leading order enter the general cross section scaled by a single polarization of either beam, target or recoil (Σ , T , P), and three sets of four asymmetries whose leading dependence in the general cross section involves two polarizations of either beam-target (E , G , F , H), beam-recoil (C_x , C_z , O_x , O_z) or target-recoil (L_x , L_z , T_x , T_z). However, each of these observables enters the general form of the cross section scaled by two terms containing different combinations of beam, target and recoil spins [16]. This leads to two distinct ways to measure each observable. The full set are summarized in Table 1. There, a caret (^) is used to designate the numerator of an asymmetry, $\hat{A} = A \cdot \sigma_0$. The bottom four rows correspond to different states of beam polarization, either without regard to incident polarization (*unpol*) or in one of the three standard *Stokes* conditions that characterize the possible polarizations of an ensemble of photons, linear with a $\sin(2\phi_\gamma)$ dependence relative to the reaction plane, linear with a $\cos(2\phi_\gamma)$ dependence, or circular. The columns of the table give the polarization of the target, recoil, or target+recoil combination. The signs indicate the sign of the corresponding term entering the general cross section. One can readily construct from this table the terms that enter the general cross section for any given combination of polarization conditions. For example, with linear beam polarization in or perpendicular to the reaction plane, a longitudinally polarized target (along z) and an analysis of recoil polarization along the meson momentum (z'), the general cross section is given by terms in the first (*unpol*) and third rows that are either independent of target and recoil polarization (σ_0 , Σ) or in columns associated with polarization along z and/or z' ,

Table 1. Polarization observables in pseudoscalar meson photo-production. Each appears twice here. Carets (^) designate the products of asymmetries with the cross section, $\hat{A} = A \cdot \sigma_0$. The 16 in black indicate the leading polarization dependence of each observable to the cross section. The three in red (P , T , Σ) are nominal *single-polarization* quantities that can be measured with double-polarization. Those in blue are the unpolarized cross section and 12 nominal *double-polarization* quantities that can be measured with triple-polarization. Signs indicate the sign of each term as it enters the general cross section (from [16]).

	Target (P^T)			Recoil (P^R)			Target (P^T) + Recoil (P^R)								
	x	y	z	x'	y'	z'	x'	x'	x'	y'	y'	y'	z'	z'	z'
γ beam (P^γ)	x	y	z				x	y	z	x	y	z	x	y	z
<i>unpol</i> : σ_0		\hat{T}			\hat{P}		\hat{T}_x		\hat{L}_x		$\hat{\Sigma}$		\hat{T}_z		\hat{L}_z
$P_L^\gamma \sin 2\phi_\gamma$:	\hat{H}		\hat{G}	\hat{O}_x		\hat{O}_z		\hat{C}_z		\hat{E}		\hat{F}		$-\hat{C}_x$	
$P_L^\gamma \cos 2\phi_\gamma$:	$-\hat{\Sigma}$		$-\hat{P}$		$-\hat{T}$		$-\hat{L}_z$		\hat{T}_z		$-\sigma_0$		\hat{L}_x		$-\hat{T}_x$
<i>cir</i> P_c^γ :		\hat{F}		$-\hat{E}$		\hat{C}_x		$-\hat{O}_z$		\hat{G}		$-\hat{H}$		\hat{O}_x	

$$d\sigma(P^\gamma, P^T, P^R) = \frac{1}{2} \left\{ \left[\sigma_0 + P_z^T P_z^R \hat{L}_{z'} \right] + P_L^\gamma \cos(2\phi_\gamma) \left[-\hat{\Sigma} - P_z^T P_z^R \hat{T}_{x'} \right] \right\} .$$

The initial factor of $\frac{1}{2}$ is always present and ensures that the unpolarized cross section is recovered when averaging over initial states.

There is some confusion in the literature regarding definitions of asymmetries and the conventions used in partial wave analyses (PWA). This arises from the use of different coordinate systems and because the same symbol or *asymmetry name* has been used by different authors to refer to different experimental quantities. Expressions for the photo-production asymmetries as coordinate-system independent ratios of cross sections, along with the names used for these ratios by different PWA groups, can be found in ref [17]. Examples of the explicit measurements needed to construct all of the observables are given in the appendices to ref [16].

4. The special role of Recoil Polarization

In pseudoscalar meson photo-production, the beam, target and recoil baryon can all be polarized, although these polarizations are not all on an identical footing. While the beam and target polarization are under experimental control, the recoil polarization is rather a by-product of the entrance channel angular momentum and the reaction physics. Expressions for the recoil polarization can be derived by grouping together the terms in the general cross section that dependent upon the components of the recoil polarization vector [16],

$$d\sigma^{\text{B,T,R}}(\vec{P}^\gamma, \vec{P}^T, \vec{P}^R) = \frac{1}{2} [A^0 + (P_{x'}^R)A^{x'} + (P_{y'}^R)A^{y'} + (P_{z'}^R)A^{z'}],$$

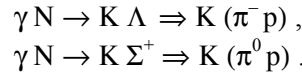
where,

$$\begin{aligned} A^0 &= d\sigma_0 - P_L^\gamma \cos(2\phi_\gamma) \hat{\Sigma} + P_y^T \hat{T} - P_L^\gamma P_y^T \cos(2\phi_\gamma) \hat{P} - P_c^\gamma P_z^T \hat{E} + P_L^\gamma P_z^T \sin(2\phi_\gamma) \hat{G} \\ &\quad + P_c^\gamma P_x^T \hat{F} + P_L^\gamma P_x^T \sin(2\phi_\gamma) \hat{H}, \\ A^{x'} &= P_c^\gamma \hat{C}_{x'} + P_L^\gamma \sin(2\phi_\gamma) \hat{O}_{x'} + P_z^T \hat{L}_{x'} + P_x^T \hat{T}_{x'} + P_L^\gamma P_y^T \sin(2\phi_\gamma) \hat{C}_{z'} - P_c^\gamma P_y^T \hat{O}_{z'} \\ &\quad - P_L^\gamma P_x^T \cos(2\phi_\gamma) \hat{L}_{z'} + P_L^\gamma P_z^T \cos(2\phi_\gamma) \hat{T}_{z'}, \\ A^{y'} &= \hat{P} + P_y^T \hat{\Sigma} - P_L^\gamma \cos(2\phi_\gamma) \hat{T} - P_L^\gamma P_y^T \cos(2\phi_\gamma) d\sigma_0 + P_L^\gamma P_x^T \sin(2\phi_\gamma) \hat{E} + P_c^\gamma P_x^T \hat{G} \\ &\quad + P_L^\gamma P_z^T \sin(2\phi_\gamma) \hat{F} - P_c^\gamma P_z^T \hat{H}, \\ A^{z'} &= P_c^\gamma \hat{C}_{z'} + P_L^\gamma \sin(2\phi_\gamma) \hat{O}_{z'} + P_z^T \hat{L}_{z'} + P_x^T \hat{T}_{z'} - P_L^\gamma P_y^T \sin(2\phi_\gamma) \hat{C}_{x'} + P_c^\gamma P_y^T \hat{O}_{x'} \\ &\quad + P_L^\gamma P_x^T \cos(2\phi_\gamma) \hat{L}_{x'} - P_L^\gamma P_z^T \cos(2\phi_\gamma) \hat{T}_{x'}. \end{aligned}$$

With this arrangement it is straight forward to show that the components of the recoil polarization vector are given by [16],

$$P_{x'}^R = \frac{A^{x'}}{A^0}, \quad P_{y'}^R = \frac{A^{y'}}{A^0}, \quad P_{z'}^R = \frac{A^{z'}}{A^0}.$$

This can lead to a particularly fruitful arena in which different components of the recoiling baryon's polarization determine various spin observables. The two most practical reactions for this are in KY production, where the angular distribution in the weak decay of the hyperon provides a self-analysis of the polarization,



The $K \Lambda$ channel has an analyzing power of about $2/3$ while that of the $K\pi^0 p$ decay branch in the $K \Sigma^+$ channel is almost unity. When a quasi- 4π detector is used, such as the CLAS at Jefferson Lab, recoil polarization information is in the data stream and comes without a significant penalty in statistics.

It is straight forward to use the above expressions to deduce observables involving recoil polarization. The simplest case occurs when neither the beam nor the target are polarized. Then the y component of the recoil polarization nonetheless survives and is determined by the observable P . This is a recoil polarization generated solely by the reaction physics and can be non-zero. An example from the $\gamma p \rightarrow K^+ \Lambda \rightarrow K^+ \pi^- p$ reaction is shown schematically in figure 6. In the rest frame of the Λ , the angular distribution of its weak decay into $\pi^- p$ takes the form,

$$W(\theta_p) = \frac{1}{2} (1 + \alpha |\vec{P}_\Lambda| \cos(\theta_p)).$$

Here θ_p is the angle between the proton direction and the normal to the reaction plane in the rest frame of the Λ and α is the Λ decay parameter, $\alpha = 0.642 \pm 0.013$. Since the cosine function changes sign between quadrants, a measurement of the recoil polarization consists in simply counting protons above and below the reaction plane.

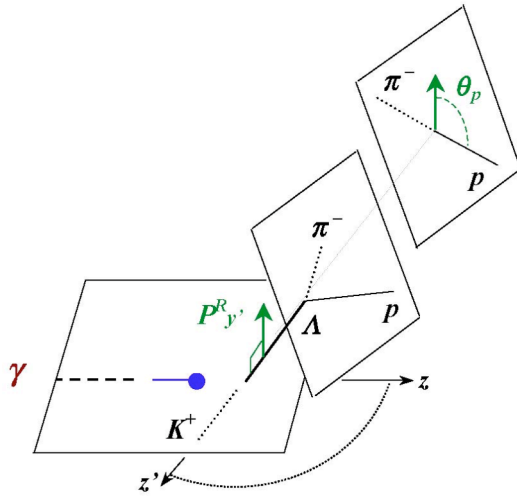


Figure 6. With beam and the target unpolarized the recoil polarization can only be perpendicular to the reaction plane, $\vec{P} = (0, P, 0)$ and is determined by the proton yields on either side of the reaction plane,

$$P = \frac{2}{\alpha} \frac{N_{up} - N_{dwn}}{N_{up} + N_{dwn}}.$$

As an example of this technique, recent measurements of the recoil asymmetry P are plotted in figure 7 for $W=1728$ MeV in the $\gamma p \rightarrow K^+ \Lambda$ reaction. The data were collected in the *BGO-Ball* at GRAAL [18] and with the CLAS detector at Jefferson Lab [19]. As mentioned above, with quasi- 4π detectors the weak decay information is in the data stream and quite accurate results can readily be obtained.

Several other examples with different experimental conditions are worked out in ref [16]. The most fruitful conditions arise when both the beam and the target are polarized. Then, the recoil polarization contains a wealth of information. For example, when circularly polarized photons are used with a longitudinally polarized target (with target spin along the beam direction), the above equations determine the components of the recoil polarization as,

$$\vec{P}^R = \left(\frac{P_c^y C_x + P_z^T L_x}{1 - P_c^y P_z^T E}, \frac{P - P_c^y P_z^T H}{1 - P_c^y P_z^T E}, \frac{P_c^y C_z + P_z^T L_z}{1 - P_c^y P_z^T E} \right).$$

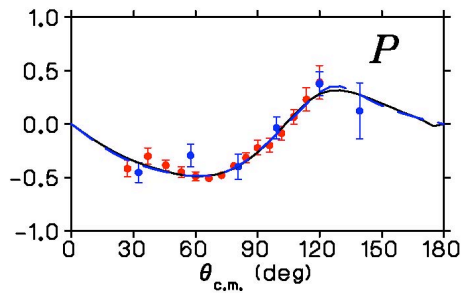


Figure 7. The recoil polarization asymmetry in the $\gamma p \rightarrow K^+\Lambda$ reaction at $W=1728$ MeV. Blue data points are GRAAL measurements from [18]; red data are CLAS results from [19].

The asymmetry in the denominator (E in red above) and the 6 observables in the numerator (in blue) can be extracted from successive analyses of the data set by choosing subsets with different spin orientations. When the recoil polarization is ignored and final states are summed, yields with the beam and target spins anti-parallel and parallel determine the E asymmetry and the denominator in the above relations. Combining flux-weighted subsets of data with opposite target polarizations, $\pm P_z^T$, determines C_x , P and C_z . Another pass through the data to average initial beam polarization states, $P_c^\gamma (h = \pm 1)$, then determines L_x and L_z . Finally, the difference between flux-weighted subsets with beam and target spins parallel and antiparallel, $P_c^\gamma (P_{+z}^T - P_{-z}^T)$, determines the H asymmetry. Interestingly, H is traditionally discussed as a *Transverse Target* asymmetry, since it appears in the second observable column of Table 1. Here, it is constructed from measurements with a longitudinally polarized target, utilizing its appearance in the forth-last column. In a similar manner, utilizing also linearly polarized beams, all 16 observables can be measured with a single target orientation [16].

5. The FROST and HDice experiments at Jefferson Lab

The key to determining complete sets of observables are triple polarization measurements. Circularly polarized photon beams are routinely created by the bremsstrahlung of longitudinally polarized electrons and linear beam polarization is generated through coherent bremsstrahlung in single crystals. As we have seen above, the analysis of weak decays in quasi- 4π detectors determines recoil polarization. The most challenging aspect of such experiments is the polarized target.

At Jefferson Lab, the $g9$ experimental runs focused on proton reactions and utilized a frozen-spin target (“FROST”) of butanol, C_4H_9OH . Here, the electrons of butanol were polarized at 0.4K and 5 tesla, after which their polarization was transferred to the ten free H atoms of the molecule using a microwave transition. A subsequent drop in temperature to the 30 mK range produced a target with a relaxation time of about 100 days with a holding field of 0.5 tesla. This process was repeated about once per week to keep the butanol polarization high. This approximate *frozen-spin* state was used in two sets of experiments, with the H polarization held either along or transverse to the beam, respectively. Typical proton polarizations were at least 80% for the 10 free H nuclei in the mass 74 butanol molecule. Carbon foils were used to estimate the background contributions from the unpolarizable materials. Both $g9$ runs can be expected to independently yield a complete set of asymmetries for the $\gamma p \rightarrow K^+\Lambda$ channel.

Since the electromagnetic interaction does not conserve isospin, measurements with both proton and neutron targets are needed to completely specify the amplitude. For polarized neutron experiments, the recently completed JLab $g14$ run used a target of molecular deuterium-hydride (“HDice”) in the solid phase. These targets have many attractive features but are considerably more complex. The HD is initially loaded with small impurities (at the $\sim 10^{-3}$ level) of H_2 and D_2 . The first rotational states of these impurities are initially populated and metastable and polarize rapidly at the 0.010K and 15 tesla conditions of a large dilution refrigerator. The H_2 and D_2 spins exchange with spins of H and D in HD and then repolarize until all of the HD reaches high polarization. With time (\sim a few months) the populations of the H_2 and D_2 rotational states decay to their magnetically inert ground states. At that point, the HD is in a true *frozen spin* state and can be transferred to an in-beam cryostat for

experiments where relaxation times are essentially unmeasurable (~years) at temperatures below 0.1K and fields of 0.8 tesla. Initial H and D polarizations were typically 60% for the H and 15% for the D. However, spins can then be transferred between H and D with RF transitions. Since the g14 run focused on polarized neutron reactions, $H \Rightarrow D$ spin transfer was used and D polarizations up to 27% were achieved. Background reactions from the unpolarizable material of the target cell were small and could be directly measured by warming the target cell and pumping out the HD gas. The product of polarization and dilution (of unpolarizable material) in the HDice and FROST targets were comparable. Nonetheless, an order of magnitude higher rates could be used with HDice before reaching data acquisition limits, due to the reduced background of atomic electrons associated with the lower Z of this target. A single target orientation was used during the g14 run (along the beam direction) and is expected to yield a complete set of asymmetries for the $\gamma n \rightarrow K^0 \Lambda$ channel.

Results for $\gamma p \rightarrow K^+ \Lambda$ from the *g1c* and *g11a* running periods at Jefferson Lab using the CLAS with liquid hydrogen have already provided the cross section, P , C_x and C_z [19, 20] data. The inclusion of these in the Bonn-Gatchina PWA has lead to possible candidates for *new* states [21], although the solutions are still ambiguous. The CLAS *g8* period ran with linear photon polarization from coherent bremsstrahlung to measure Σ , T , P , O_x and O_z and these results are nearly finalized. Once the analyses of these measurements and the *g9* and *g14* results are complete, the results are expected to have dramatic impacts on deduced multipoles and on our understanding of the N^* spectrum.

6. Amplitude extraction and uniqueness

Each of the 16 spin observables can be written in terms of 4 complex amplitudes, which can be expressed in ether Cartesian (F_i) [22], Spherical or Helicity (H_i), or Transversity (b_i) representations [23]. An explicit decomposition of all 16 into the 4 CGLN F_i amplitudes is given in [16]. However, the four amplitudes in each of these representations are angle dependent. Extracting them directly from experiment would require separate fits at each angle, which greatly limits the data that can be used and requires some model-dependent scheme to constrain an arbitrary phase that could be angle-dependent. The solution to this intractable situation is a *Wigner-Echart* style factorization into reduced matrix elements, or *multipoles*, and simple angle-dependent coefficients from angular momentum algebra [16,22]. One can then fit the multipoles directly, which both facilitates the search for resonance behavior and allows the use of full angular distribution data at a fixed energy to constrain angle-independent quantities. The price is a significant increase in the number of fitting parameters, but since the excited states of the nucleon are associated with discrete values for their angular momentum, this expansion of variables is inevitable.

Since the full amplitude is a sum of four independent complex terms, measurements of eight different observables are needed for a mathematical solution. (In practice, given realistic uncertainties on data, many more are required. But more on that later.) Since there are a total of 16 spin observables, it is clear that they are not all independent. A set of 37 *Fierz Identities* interrelate the spin asymmetries [13,16]. With a full suite of polarization data, the complete set of Fierz identities can be used to almost eliminate systematic scale shifts between data sets. However, utilizing them requires data sets at common angles and energies, which in practice requires some interpolation.

A critical issue for the goal of determining an amplitude is the uniqueness of the solution. The reaction channel with the largest number of different observables published to date is $\gamma p \rightarrow K^+ \Lambda$, where results from GLAS *g1c* and *g11* [20,19] and from GRAAL [18,24] can be combined to provide values for eight observables $\{\sigma, \Sigma, T, P, O_x, O_z, C_x$ and $C_z\}$ over at least a limited W range, 1676 to 1883 MeV. We have carried out a multipole analysis for this combined set using a Monte Carlo sampling of the parameter space, coupled with gradient minimization [16]. These CLAS and GRAAL results determine bands of solutions, that are indistinguishable in their ability to reproduce the data but nonetheless derive from very different multipole amplitudes. As an example, data at $W = 1883$ MeV are plotted in figure 8 and compared to multipole solutions having the minimum (0.74) and largest

(0.92) χ^2/point . The corresponding solution bands are shown for multipoles up to $L=2$ in figure 9. The bands represent a shallow χ^2 valley pitted with a large number of local minima that are experimentally degenerate [16]. Evidently much more information will be required for a well-defined solution.

Amplitudes can of course be rotated by an arbitrary phase. There are two methods to remove such ambiguities. The simplest is to set the phase of one particular multipole to zero, and it helps to choose a relatively large one (eg. the E_{0+} , as has been done in the fits of figures 8 and 9). This does not generally limit the utility of a solution. To compare with results from other PWA one simply rotates all solutions

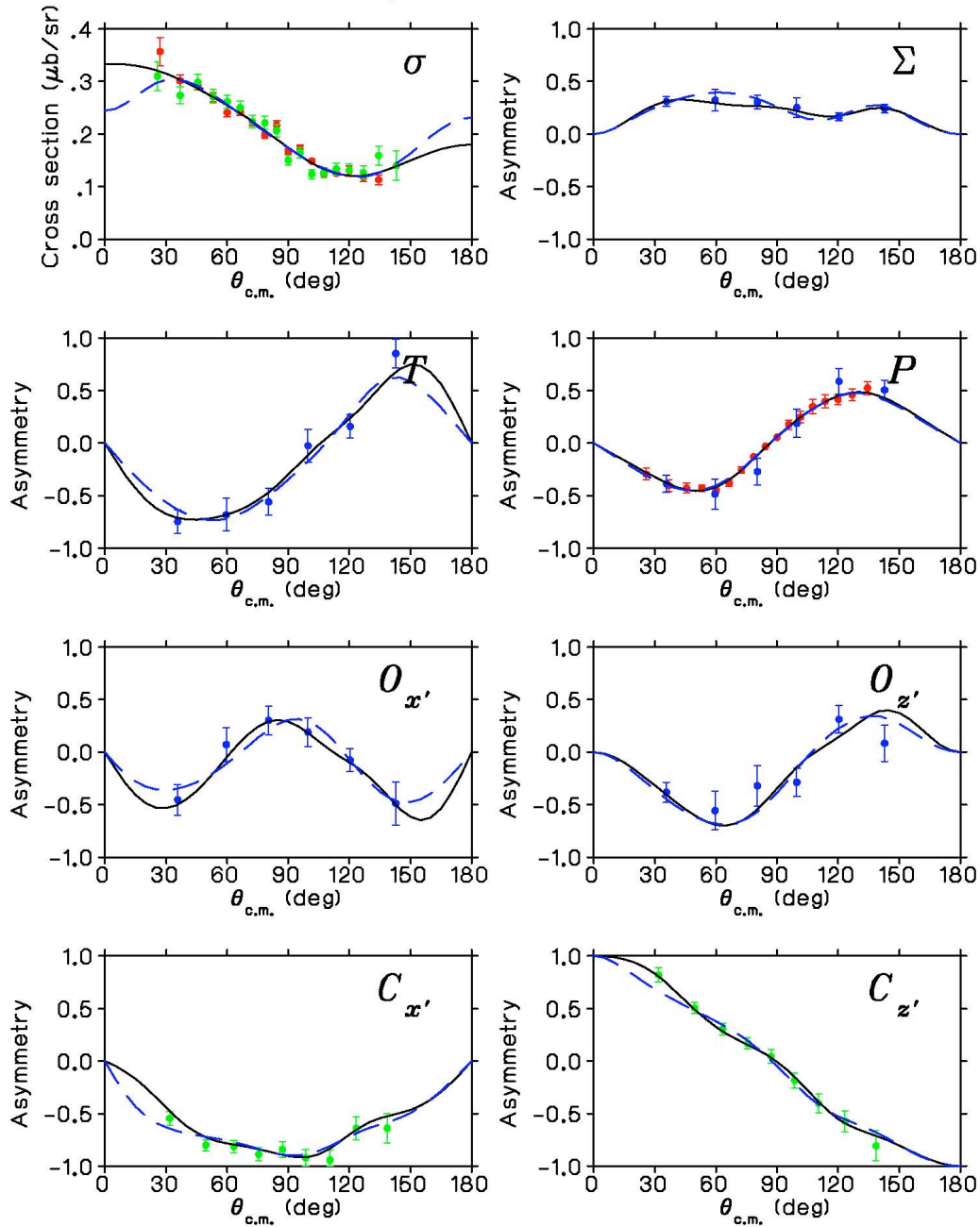


Figure 8. $\gamma p \rightarrow K^+ \Lambda$ results from [20], [19], [18] and [24] at $W=1883$ MeV. The solid (black) and long-dashed (blue) curves are multipole fits with the lowest (0.74) and largest (0.92) χ^2/point .

to the same reference phase. (eg. Multiply all multipoles of another solution by $e^{-i\phi}$, where ϕ is the phase of the E_{0+} in that solution.) Another method of fixing the overall phase that has been successfully used in charged π production is to set high L multipoles to their real Born and t -channel pole values [25]. The t -channel graphs for π photo-production have significant well-established contributions that extent to very high L and these essentially determine the phase. Unfortunately, in K^+ production this procedure isn't directly applicable for several reasons: the t -channel couplings are much smaller (being inversely proportional to the mass of the exchanged meson), there are more meson candidates that can

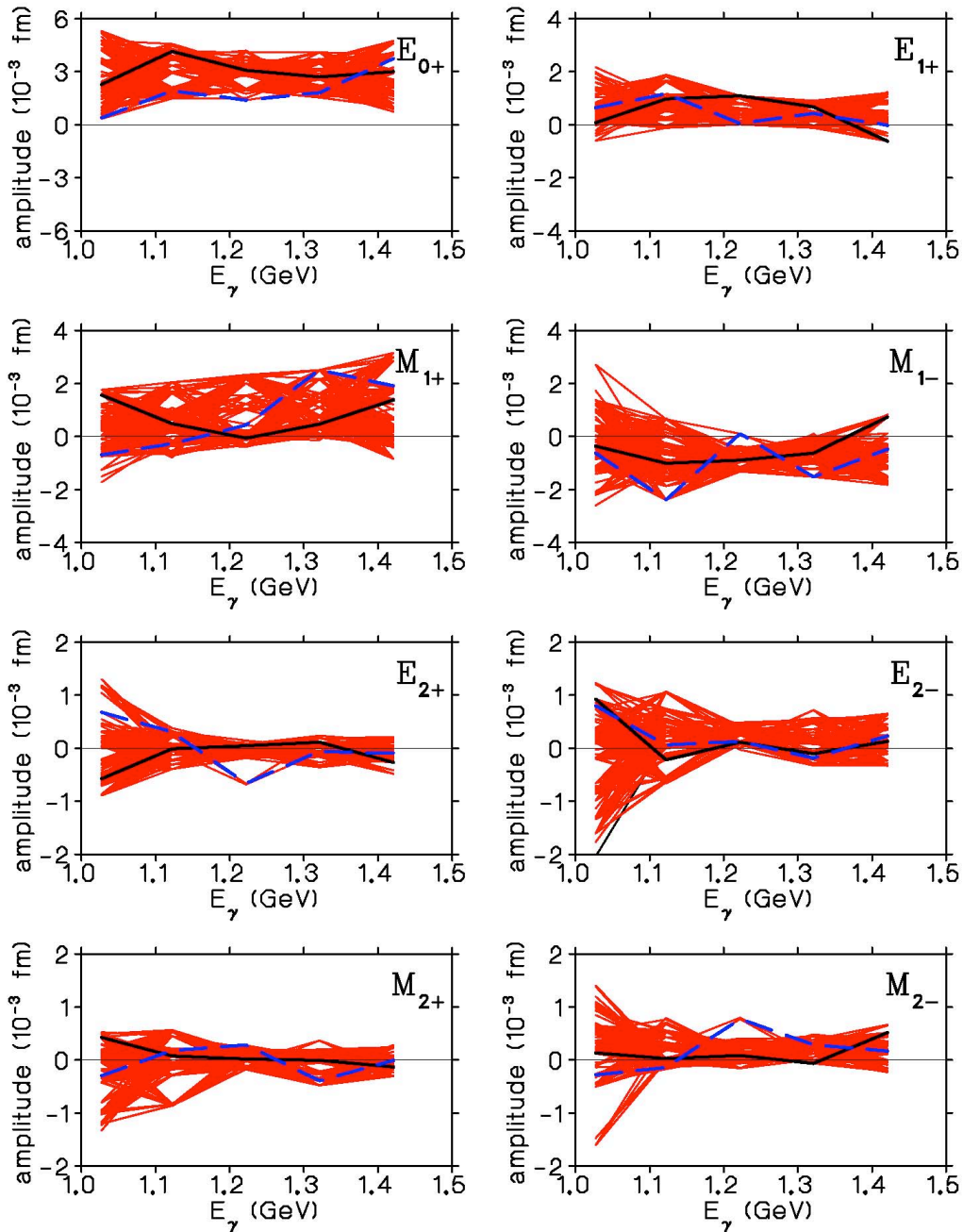


Figure 9. Real parts of the fitted multipoles for $L=0, 1, 2$ fitted to published data from [18,19,20,24], with the phase of the E_{0+} multipole fixed to zero [16]. The bands show variations in the χ^2/point of less than 0.2. Solutions with the smallest and largest χ^2/point are shown as the solid (black) and long-dashed (blue) curves, respectively.

be exchanged that are close in mass $\{K^+(493), K^*(892), K_1(1270)$ and $K_1(1400)\}$ and their couplings are not well known. Thus, for the hyperon channel with the greatest potential to supply a complete set of observables, one will always have to fix the phase of one particular multipole.

We have simulated the ultimate data sets we expect to have available in studies of pseudo-data [16]. Asymmetries were generated from a reference multipole solution at the angles and energies of the CLAS measurements, and then dithered about those points by smearing with Gaussians of width given by the expected experimental errors. Multiple local minima are always present, arising essentially from experimental uncertainties. Nonetheless, very significant gains in narrowing of the solution bands come from the addition of new spin observables. Often, even modest errors on an asymmetry are sufficient to derive a substantial gain. It is clear that the criteria for a mathematical solution that have been discussed in the literature [13,23] are unfortunately broken by measurement errors in realistic experiments. Nonetheless, studies with mock-data on a complete suite of 16 observables, accompanied by the uncertainties expected from the recently completed measurements, do result in a dramatic narrowing of the multipole uncertainty bands [16].

7. Summary and outlook

The recent confirmation from LQCD calculations of a large number of as yet unidentified excited nucleon levels has shifted the focus of nucleon structure from speculating why more states might not exist to a concerted effort to find them. Indeed, a failure to locate more than what had been observed in πN scattering would pose a serious problem. New candidates have been proposed, mainly based on recoil polarization asymmetries in hyperon photo-production, although the amplitude solutions remain ambiguous. Given realistically achievable uncertainties, the number of spin asymmetries needed to remove ambiguities in the determination of photo-production amplitudes is many more than the 8 required for an *in principle* mathematical solution. Hyperon channels, particularly $K\Lambda$ and $K\Sigma^+$ offer the potential for accumulating data on all 16 photo-production spin observables and there now exist large new data sets which are currently under analysis. These are expected to provide a determination of the production amplitudes with minimal uncertainty spread, and these in turn will form the ultimate starting point in a search for new N^* poles by analytic continuation. We expect this to create a watershed in our understanding of the nucleon spectrum.

Acknowledgments

The author wishes to thank Drs. T-S. Harry Lee, Sam Hoblit and Craig Roberts for many useful discussions. This work was supported by the US Department of Energy, Office of Nuclear Physics Division, under contract DE-AC05-06OR23177 under which Jefferson Science Associates operate Jefferson Laboratory.

References

-
- [1] Bhagwat M S, Pichowsky M A, Roberts C D and Tandy P C, 2003 *Phys. Rev.* **C68** 015203
 - [2] Capstick S and Roberts W, 1998 *Phys. Rev.* **D58** 074011
 - [3] Anselmino M *et al.*, 1993 *Rev. Mod. Phys.* **65**, 1199; and references therein
 - [4] Maris P, 2004 *Few Body Systems* **35**, 117
 - [5] Edwards R G, Dudek J J, Richards D G and Wallace S J, 2011 *Phys. Rev.* **D84** 074508
 - [6] Roper L D, 1964 *Phys. Rev. Lett.* **12** 340
 - [7] Arndt R A, Briscoe W J, Strakovsky I I and Workman R L, 2006 *Phys. Rev.* **C74** 045205
 - [8] Aznauryan I G, *et al* (CLAS Collaboration), 2009 *Phys. Rev.* **C80** 055203
 - [9] Mokeev V I, *et al* (CLAS Collaboration), 2012 *Phys. Rev.* **C86** 035203, and references therein
 - [10] Li Z, Burkert V and Li Z, 1992 *Phys. Rev.* **D46** 70
 - [11] Julia-Diaz B, *et al* (EBAC), 2008 *Phys. Rec.* **C77** 045205
 - [12] Suzuki N *et al* (EBAC), 2010 *Phys. Rev. Lett.* **104** 042302
 - [13] Chaing W-T and Tabakin F, 1997 *Phys. Rev.* **C55** 2054

-
- [14] The g9-Frost series of experiments, < <http://clasweb.jlab.org/shift/g9/>>
 - [15] The g14-HDice experiment, < http://www.jlab.org/exp_prog/proposals/06/PR-06-101.pdf>
 - [16] Sandorfi A M, Hoblit S, Kamano H and Lee T-S H, 2011 *J. Phys.* **G38**, 053001
 - [17] Sandorfi A M, Dey B, Sarantsev A, Tiator L and Workman R, arXiv:1108.5411v2
 - [18] Lleres A *et al* (GRAAL Collaboration), 2007, *Eur. Phys. J.* **A31** 79
 - [19] McCracken M E *et al* (CLAS Collaboration), 2011 *Phys. Rev.* **C81** 025201
 - [20] Bradford R K *et al* (CLAS Collaboration), 2006 *Phys. Rev.* **C73** 035202; *ibid*, 2007 **C75** 035205.
 - [21] Anisovich A V, Beck R, Klempt E, Nikonov V A, Sarantsev A V and Thoma U, 2012, *Eur. Phys. J.* **A48**, 14
 - [22] Chew G, Goldberger M, Low F and Nambu Y, 1957 *Phys. Rev.* **105** 1345
 - [23] Barker I, Donnachie A and Storrow J, 1975 *Nucl. Phys.* **B95** 347
 - [24] Lleres A *et al* (GRAAL Collaboration), 2009, *Eur. Phys. J.* **A39** 149
 - [25] Workman R L, *priv. comm.*